Charge density wave order on a π-flux square lattice

Y.-X. Zhang,[1,*] H.-M. Guo,[2] and R. T. Scalettar[1]
[1]*Department of Physics, University of California, Davis, California 95616,USA*
[2]*Department of Physics, Key Laboratory of Micro-nano Measurement-Manipulation and Physics (Ministry of Education), Beihang University, Beijing 100191, China*

(Received 24 February 2020; revised manuscript received 7 May 2020; accepted 8 May 2020; published 21 May 2020)

The effect of electron-phonon coupling on Dirac fermions was recently explored numerically on a honeycomb lattice, leading to precise quantitative values for the finite temperature and quantum critical points. In this paper, we use the unbiased determinant quantum Monte Carlo method to study the Holstein model on a half-filled staggered-flux square lattice and compare the results with the honeycomb lattice geometry, presenting results for a range of phonon frequencies $0.1 \leqslant \omega \leqslant 2.0$. We find that the interactions give rise to charge density wave order, but only above a finite coupling strength λ_{crit}. The transition temperature is evaluated and presented in a T_c-λ phase diagram. An accompanying mean-field theory calculation also predicts the existence of a quantum phase transition, but at a substantially smaller coupling strength.

DOI: 10.1103/PhysRevB.101.205139

I. INTRODUCTION

The physics of massless Dirac points, as exhibited in the band structure of the honeycomb lattice of graphene, has driven intense study [1–4]. The square lattice with π flux per plaquette is an alternate tight-binding Hamiltonian which also contains Dirac points in its band structure. Initial investigations of the π-flux model focused on the noninteracting limit [5], but as with the honeycomb lattice, considerable subsequent effort has gone into extending this understanding to incorporate the effect of electron-electron interactions. Numerical simulations of the Hubbard Hamiltonian with an on-site repulsion U between spin-up and spin-down fermions, including exact diagonalization [6] and quantum Monte Carlo (QMC) [7–14], revealed a quantum phase transition at $U_c \sim 5.55t$ into a Mott antiferromagnetic (AF) phase in the chiral Heisenberg Gross-Neveu universality class. For a spinless fermion system with near-neighbor interactions a chiral Ising Gross-Neveu universality class is suggested [15]. These results have been contrasted with those on a honeycomb lattice, which has a similar Dirac point structure, although at a smaller critical interaction $U_c \sim 3.85t$ [11].

In the case of the repulsive Hubbard Hamiltonian, there were two motivations for studying both the honeycomb and the π-flux geometries. The first was to verify that the quantum critical transitions to AF order as the on-site repulsion U increases share the same universality class, that of the Gross-Neveu model. The second was to confirm that an intermediate spin-liquid phase between the semimetal and AF phases [16], which had been shown not to be present on a honeycomb lattice [17], was also absent on the π-flux geometry.

Studies of the SU(2) π-flux Hubbard model have also been extended to SU(4), using projector QMC [18], and to staggered flux where $\pm\pi$ hopping phases alternate on the lattice [19]. In the former case, the semimetal to AF order transition was shown to be replaced by a semimetal to valence bond solid transition characterized by breaking of a $\mathcal{Z}_4$ symmetry. In the latter work, an intermediate phase with power-law decaying spin-spin correlations was suggested to exist between the semimetal and AF.

A largely open question is how this physics is affected in the presence of electron-phonon rather than electron-electron interactions. A fundamental Hamiltonian, proposed by Holstein [20], includes an on-site coupling of electron density to the linear displacement of the phonon field. In the low-density limit, extensive numerical work has quantified polaron and bipolaron formation, in which electrons are "dressed" by an accompanying lattice distortion [21–28]. At sufficiently large coupling, electrons or pairs of electrons can become "self-trapped" (localized). One of the most essential features of the Holstein model is that the lattice distortion of one electron creates an energetically favorable landscape for other electrons, so that there is an effective attraction mediated by the phonons. At higher densities, collective phenomena such as charge density wave (CDW) phases and superconductivity (SC) have been widely studied [24,29–36]. The CDW is especially favored on bipartite lattices and at fillings which correspond to double occupation of one of the two sublattices. SC tends to occur when one dopes away from these commensurate fillings.

Recent work on the Holstein model on the honeycomb lattice suggested a quantum phase transition from semimetal to gapped CDW order [37,38], similar to the results for the Hubbard Hamiltonian. However, a key difference between the Hubbard and Holstein models is the absence of the SU(2) symmetry of the order parameter in the latter case. Thus, while long-range AF order arising from electron-electron interaction occurs only at zero temperature in two dimensions, the CDW phase transition induced by electron-phonon coupling can

*zyxzhang@ucdavis.edu

occur at finite temperature: the symmetry being broken is that associated with two *discrete* sublattices. For classical phonons ($\omega_0 = 0$), the electron-phonon coupling becomes an on-site energy in the mean-field approximation. In the antiadiabatic limit where phonon frequencies are set to infinity, the Holstein model maps to the attractive Hubbard model.

Here we extend the existing work on the effect of electron-phonon coupling (EPC) on Dirac fermions from the honeycomb geometry to the π-flux lattice. The π-flux state is realized by threading half of a magnetic flux quantum through each plaquette of a square lattice [39]. Recently, it was experimentally realized in optical lattices using Raman-assisted hopping [40]. There are also theoretical suggestions that the π-flux lattice might be engineered by the proximity of an Abrikosov lattice of vortices of a type-II superconductor or via spontaneously generating a π flux by coupling fermions to a $\mathcal{Z}_2$ gauge theory in $(2+1)$ dimensions [41]. The π-flux hopping configuration has an additional interesting feature motivating our current work: it is the unique magnetic field value which minimizes the ground-state energy for noninteracting fermions at half-filling on a bipartite lattice. Indeed, Lieb showed that this theorem is also true at finite temperature and furthermore holds in the presence of Hubbard interactions [42]. Here we consider the thermodynamics of the π-flux lattice with EPC.

This paper is organized as follows: in the next section, we describe the Holstein model and the π-flux square lattice. Section III presents, briefly, a mean-field theory (MFT) for the model. Section IV reviews our primary method, determinant quantum Monte Carlo (DQMC). Section V contains results from the DQMC simulations, detailing the nature of the CDW phase transition, both the finite-temperature transition at fixed EPC and the quantum phase transition, which occurs at $T = 0$ with varying EPC. Section VI contains our conclusions.

II. MODEL

The Holstein model [20] describes conduction electrons locally coupled to phonon degrees of freedom,

$$\hat{\mathcal{H}} = -\sum_{\langle \mathbf{i},\mathbf{j}\rangle,\sigma} (t_{\mathbf{i},\mathbf{j}}\, \hat{d}^{\dagger}_{\mathbf{i}\sigma}\hat{d}_{\mathbf{j}\sigma} + \text{H.c.}) - \mu \sum_{\mathbf{i},\sigma} \hat{n}_{\mathbf{i},\sigma} + \frac{1}{2M}\sum_{\mathbf{i}} \hat{P}^2_{\mathbf{i}} + \frac{\omega_0^2}{2}\sum_{\mathbf{i}} \hat{X}^2_{\mathbf{i}} + \lambda \sum_{\mathbf{i},\sigma} \hat{n}_{\mathbf{i},\sigma}\hat{X}_{\mathbf{i}}. \quad (1)$$

The sums on $\mathbf{i}$ and σ run over all lattice sites and spins $\sigma = \uparrow, \downarrow$. $\langle \mathbf{i}, \mathbf{j}\rangle$ denotes nearest neighbors. $\hat{d}^{\dagger}_{\mathbf{i}\sigma}$ and $\hat{d}_{\mathbf{i}\sigma}$ are creation and annihilation operators of electrons with spin σ on a given site $\mathbf{i}$; $\hat{n}_{\mathbf{i},\sigma} = \hat{d}^{\dagger}_{\mathbf{i}\sigma}\hat{d}_{\mathbf{i}\sigma}$ is the number operator. The first term of Eq. (1) corresponds to the hopping of electrons $\mathcal{K}_{\text{el}}$, with chemical potential μ. The next line of the Hamiltonian describes optical phonons, local quantum harmonic oscillators of frequency ω_0, and phonon position and momentum operators, $\hat{X}_{\mathbf{i}}$ and $\hat{P}_{\mathbf{i}}$, respectively. The phonons are dispersionless since there are no terms connecting $\hat{X}_{\mathbf{i}}$ on different sites of the lattice. The phonon mass M is set to unity. The electron-phonon coupling is included in the last term. We set hopping $|t_{\mathbf{i},\mathbf{j}}| = t = 1$ as the energy scale and focus on half-filling ($\langle \hat{n}\rangle = 1$), which can be achieved by setting $\mu = -\lambda^2/\omega_0^2$. It is useful to present results in terms of the dimensionless coupling $\lambda_D = \lambda^2/(\omega_0^2 W)$, which represents the ratio of the effective electron-electron interaction obtained after integrating out the phonon degrees of freedom, and W is the kinetic energy bandwidth.

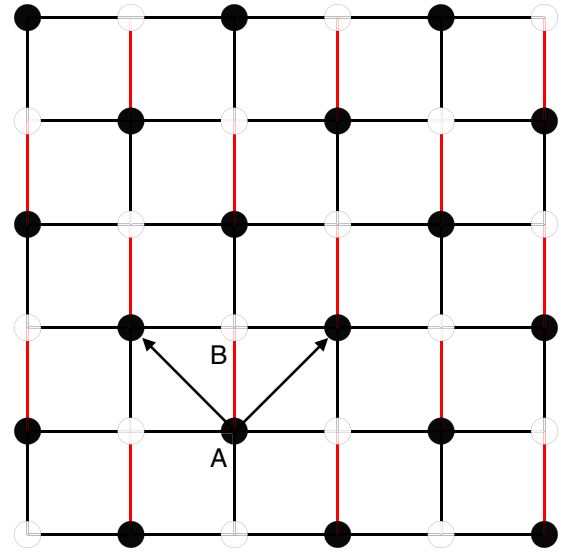

FIG. 1. π-flux phase on a 6×6 square lattice. Sublattices A and B are shown by solid and open circles. Bonds in red correspond to hopping $t' = -t$, the opposite of black lines with hopping t. Arrows represent the basis vectors.

The two-dimensional π-flux phase on a square lattice is schematically shown in Fig. 1. All hoppings in the x direction are t, while half of the hoppings along the y direction are set to $t' = te^{i\pi} = -t$, where the phase π in the hopping amplitude arises from the Peierls prescription for the vector potential of the magnetic field. As a consequence, an electron hopping on a contour around each plaquette picks up a total phase π, corresponding to one half of a magnetic flux quantum $\Phi_0 = hc/e$ per plaquette. The lattice is bipartite, with two sublattices A and B. Each unit cell consists of two sites. In reciprocal space, with the reduced Brillouin zone ($|k_x| \leqslant \pi$, $|k_y| \leqslant |k_x|$), the noninteracting part of Hamiltonian (1) can be written as

$$\hat{\mathcal{H}}_0 = \sum_{\mathbf{k}\sigma} \hat{\psi}^{\dagger}_{\mathbf{k}\sigma}\mathbf{H}_0(\mathbf{k})\hat{\psi}_{\mathbf{k}\sigma}, \quad (2)$$

where

$$\hat{\psi}_{\mathbf{k}\sigma} = (\hat{d}_{A\sigma} \quad \hat{d}_{B\sigma})^T \quad (3)$$

and the noninteracting Hamiltonian matrix

$$\mathbf{H}_0(\mathbf{k}) = \begin{pmatrix} 0 & 2t\cos k_x + 2it\sin k_y \\ 2t\cos k_x - 2it\sin k_y & 0 \end{pmatrix}. \quad (4)$$

The energy spectrum $E_{\mathbf{k}} = \pm 2t\sqrt{\cos^2 k_x + \sin^2 k_y}$ describes a semimetal with two inequivalent Dirac points at $\mathbf{K}_{\pm} = (\pm\pi/2, 0)$, shown in Fig. 2. In the low-energy regime of the dispersion, the density of states (DOS) vanishes linearly near the Dirac point where $E_{\mathbf{k}} = 0$, as shown in Fig. 3. The bandwidth of the π-flux phase is $W = 4\sqrt{2}t$. In Fig. 3 the DOS of the honeycomb lattice is shown for comparison. The Dirac Fermi velocity is $v_{\text{F}} = 2t$ ($1.5t$) for the π-flux (honeycomb)

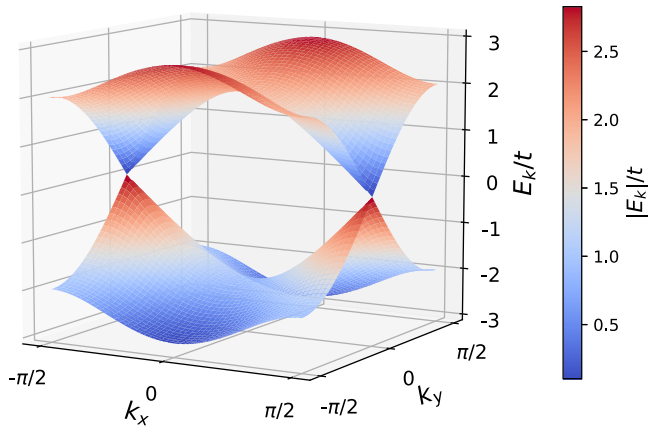

FIG. 2. The dispersion relation $E_{\mathbf{k}}$ for the π-flux phase on a square lattice. There are two Dirac points at $(k_x, k_y) = (\pm\pi/2, 0)$. The bandwidth for the π-flux model is $W = 4\sqrt{2}t$.

lattice. Near the Dirac point, the DOS $\rho(\omega) \sim |\omega|/v_{\mathrm{F}}$, and the π-flux model has a smaller slope.

III. MEAN-FIELD THEORY

In this section, we present a mean-field theory approach to solve the Holstein model. Semimetal to superfluid transitions were previously investigated with MFT in two and three dimensions [43,44]. Here we focus on the semimetal to CDW transition. In the mean-field approximation, the phonon displacement at site $\mathbf{i}$ is replaced by its average value, modulated by a term which has opposite signs on the two sublattices,

$$\langle X_{\mathbf{i}} \rangle = X_0 \pm X_{\mathrm{mf}}\,(-1)^{\mathbf{i}}. \tag{5}$$

Here $X_0 = -\lambda/\omega_0^2$ is the "equilibrium position" at half-filling, and X_{mf} is the mean-field order parameter. When $X_{\mathrm{mf}} = 0$, phonons on all sites have the same average displacement, indicating the system remains in the semimetal phase, whereas when $X_{\mathrm{mf}} \neq 0$, the last term in the Hamiltonian (1), i.e., $\lambda \sum_{\mathbf{i},\sigma} \hat{n}_{\mathbf{i},\sigma} \hat{X}_{\mathbf{i}}$, becomes an on-site staggered potential, which corresponds to the CDW phase. The phonon kinetic energy

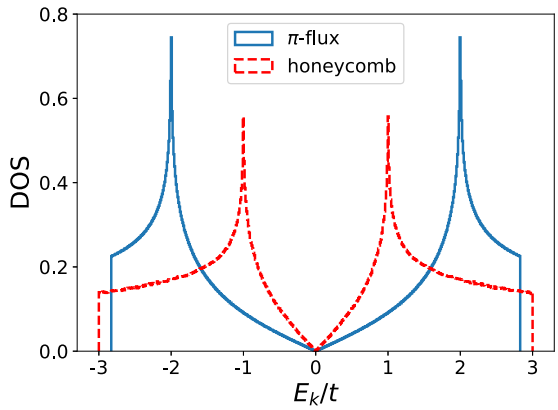

FIG. 3. The density of states for the π-flux phase square lattice and the honeycomb lattice. The bandwidths are nearly identical, but the honeycomb lattice has a substantially larger slope of the linear increase of the DOS.

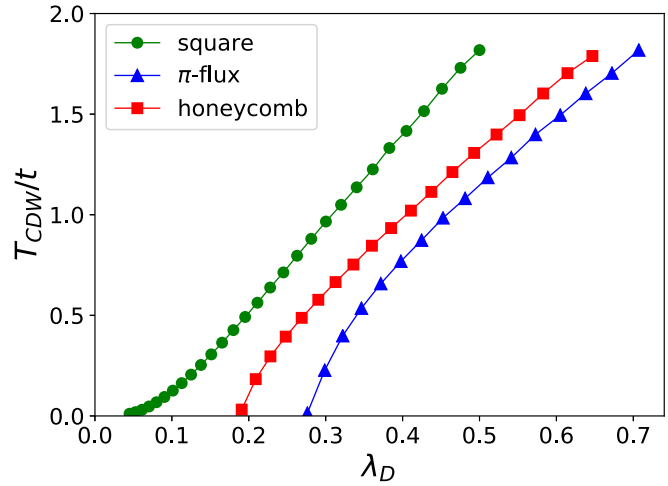

FIG. 4. MFT T_c for the CDW phase transition as a function of dimensionless coupling λ_D for the square lattice with no magnetic flux, the π-flux phase square lattice, and the honeycomb lattice. For the geometries with a Dirac spectrum MFT captures the existence for a QCP, a critical value of λ_D below which there is no CDW order even at $T = 0$, and the absence of a QCP for the conventional square lattice.

term is zero as a result of the static field. The resulting static mean-field Hamiltonian is quadratic in the fermion operators. Diagonalizing gives energy eigenvalues $\epsilon_n(X_{\mathrm{mf}})$. The free energy F can then be directly obtained by

$$F(\beta, X_{\mathrm{mf}}) = -\frac{1}{\beta}\sum_n \ln(1 + e^{-\beta\epsilon_n}) + \frac{N\omega_0^2}{2}\left(X_0^2 + X_{\mathrm{mf}}^2\right). \tag{6}$$

Minimizing the free energy with respect to X_{mf} (or, equivalently, a self-consistent calculation) will determine the order parameter. X_{mf} is found to be zero at high temperatures: the energy cost of the second term in Eq. (6) exceeds the energy decrease in the first term associated with opening of a gap in the spectrum ϵ_n. X_{mf} becomes nonzero below a critical temperature T_c.

T_c for the π-flux lattice is shown in Fig. 4, along with the result of analogous MFT calculations for the honeycomb and (zero-flux) square geometries. The lattice size $L = 180$ is chosen for all three models. This is sufficiently large that finite-size effects are smaller than the statistical sampling error bars. At zero temperature, the CDW order exhibits a critical EPC for the π-flux and honeycomb lattices. This quantum critical point (QCP) arises from the Dirac fermion dispersion, which has a vanishing DOS at the Fermi energy. The honeycomb lattice QCP has a smaller critical value. However, when measured in units of the Fermi velocity, the ratios $\lambda_{D,\mathrm{crit}}/v_{\mathrm{F}} = 0.13$ and 0.14 are quite close for the honeycomb and π-flux geometries, respectively. We will see this is also the case for the exact DQMC calculations. For the square lattice, on the other hand, the DOS has a Van Hove singularity at the Fermi energy, and the CDW develops at arbitrarily small coupling strength.

Another feature of the MFT phase diagram is that, as the coupling increases, T_c increases monotonically. This is in contrast to the exact DQMC results, where T_c decreases

at large coupling strengths. A similar failure of MFT is well known for the Hubbard Hamiltonian where the formation of AF ordering is related to two factors: the local moment $m_z^2 = (n_\uparrow - n_\downarrow)^2 = 1 - 2\langle n_\uparrow n_\downarrow \rangle$ and the exchange coupling $J \sim t^2/U$. The double occupancy $\langle n_\uparrow n_\downarrow \rangle$ is suppressed by the interaction, resulting in the growth of the local moment. Thus, upon cooling, the Hubbard model has two characteristic temperatures: the temperature of local moment formation, which increases monotonically with U, and the AF ordering scale, which falls with J. Since the interaction is simply decoupled locally and the exchange coupling is not addressed, within MFT the formation of the local moments and their ordering occur simultaneously. MFT thus predicts a monotonically increasing T_c with U.

IV. DQMC METHODOLOGY

We next describe the DQMC method [45,46]. In evaluating the partition function $\mathcal{Z}$, the inverse temperature β is discretized as $\beta = L_\tau \Delta\tau$, and complete sets of phonon position eigenstates are introduced between each $e^{-\Delta\tau \hat{\mathcal{H}}}$. The phonon coordinates acquire an "imaginary-time" index, converting the two-dimensional quantum system to a $(2+1)$-dimensional classical problem. After tracing out the fermion degrees of freedom, which appear only quadratically in the Holstein Hamiltonian, the partition function becomes

$$\mathcal{Z} = \int \mathcal{D}x_{\mathbf{i},l}\, e^{-\mathcal{S}_{ph}} [\det \mathbf{M}(x_{\mathbf{i},l})]^2, \tag{7}$$

where the "phonon action" is

$$\mathcal{S}_{ph} = \Delta\tau \left[\frac{1}{2}\omega_0^2 \sum_{\mathbf{i}} x_{\mathbf{i},l}^2 + \frac{1}{2M} \sum_{\mathbf{i}} \left(\frac{x_{\mathbf{i},l+1} - x_{\mathbf{i},l}}{\Delta\tau} \right)^2 \right]. \tag{8}$$

Because the spin-up and spin-down fermions have coupling identical to the phonon field, the fermion determinants which result from the trace are the same, and the determinant is squared in Eq. (7). Thus, there is no fermion sign problem [47]. We use $\Delta\tau = 0.1/t$, small enough that Trotter errors associated with the discretization of β are of the same order of magnitude as the statistical uncertainty from the Monte Carlo sampling.

V. DQMC RESULTS

A. Double occupancy and kinetic energy

We first show data for several local observables, the electron kinetic energy $|\mathcal{K}_{\rm el}| = |\sum_{\langle \mathbf{i},\mathbf{j}\rangle,\sigma} (t_{\mathbf{i},\mathbf{j}} \hat{d}_{\mathbf{i}\sigma}^\dagger \hat{d}_{\mathbf{j}\sigma} + \text{H.c.})|$ and double occupancy $\mathcal{D} = \langle n_{\mathbf{i}\uparrow} n_{\mathbf{i}\downarrow} \rangle$. For a tight-binding model on a bipartite lattice at half-filling, Lieb showed that the energy-minimizing magnetic flux is π per plaquette, both for noninteracting fermions and in the presence of a Hubbard U [42]. Here we show $|\mathcal{K}_{\rm el}|$ for the Holstein model, a case not hitherto considered.

Figure 5 shows $|\mathcal{K}_{\rm el}|$ (left panel) and $\mathcal{D}$ (right panel) as functions of the dimensionless EPC λ_D for $\beta = 6/t, 8/t, 10/t$. There is little temperature dependence for these local quantities. The magnitude of the kinetic energy $|\mathcal{K}_{\rm el}|$ decreases as λ_D grows, reflecting the gradual localization of the dressed electrons ("polarons").

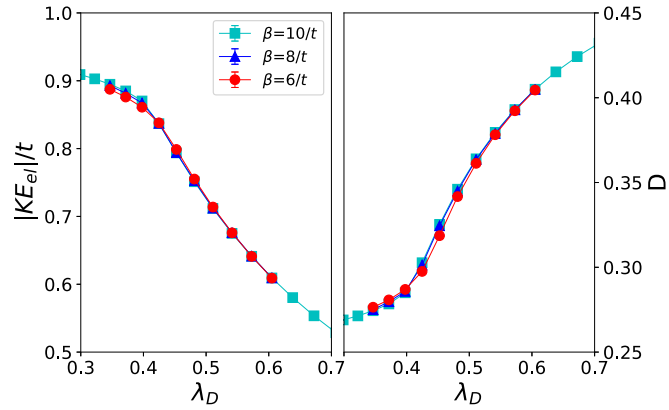

FIG. 5. Left: The magnitude of electron kinetic energy $|\mathcal{K}_{\rm el}|$ as a function of EPC strength λ_D. Simulations are performed on a $L = 10$ lattice at inverse temperatures $\beta = 6/t, 8/t, 10/t$ and fixed $\omega_0 = 1.0t$. Right: Double occupancy D as a function of EPC strength λ_D.

At the same time, the double occupancy $\mathcal{D}$ evolves from its noninteracting value $\mathcal{D} = \langle n_{\mathbf{i}\uparrow} n_{\mathbf{i}\downarrow} \rangle = \langle n_{\mathbf{i}\uparrow} \rangle \langle n_{\mathbf{i}\downarrow} \rangle = 1/4$ at half-filling to $\mathcal{D} = 1/2$ at large λ_D. In the strong-coupling regime, we expect robust pair formation, so that half of the lattice sites will be empty and half will be doubly occupied.

The evolution of $\mathcal{D}$ and $|\mathcal{K}_{\rm el}|$ has the largest slope at $\lambda_D \sim 0.42$, which, as will be seen, coincides with the location of the QCP between the semimetal and CDW phases.

B. Existence of long-range CDW order

The structure factor $S(\mathbf{Q})$ is the Fourier transform of the real-space spin-spin correlation function $c(\mathbf{r})$,

$$S(\mathbf{Q}) = \sum_{\mathbf{r}} e^{i\mathbf{Q}\cdot\mathbf{r}} c(\mathbf{r}),$$
$$c(\mathbf{r}) = \langle (n_{\mathbf{i}\uparrow} + n_{\mathbf{i}\downarrow})(n_{\mathbf{i}+\mathbf{r}\uparrow} + n_{\mathbf{i}+\mathbf{r}\downarrow}) \rangle, \tag{9}$$

and characterizes the charge ordering. In a disordered phase $c(\mathbf{r})$ is short range, and $S(\mathbf{Q})$ is independent of lattice size. In an ordered phase, $c(\mathbf{r})$ remains large out to long distances, and the structure factor will be proportional to the number of sites at the appropriate ordering wave vector $\mathbf{Q}$. At half-filling $S(\mathbf{Q})$ is largest at $\mathbf{Q} = (\pi, \pi)$. We define $S_{\rm cdw} \equiv S(\pi, \pi)$. Figure 6 displays $S_{\rm cdw}$ as a function of inverse temperature β at different phonon frequencies ω_0 and coupling strengths λ_D. The linear lattice size $L = 6$. At fixed ω_0 and strong coupling, $S_{\rm cdw}$ grows as temperature is lowered and saturates to $S_{\rm cdw} \sim N$, indicating the development of long-range order (LRO), i.e., the phase transition into the CDW phase. Note that $\beta = 10/t$ is always in the plateau region, suggesting the correlation length has become larger than the lattice size and the ground state has been reached. In the following, we use $\beta = 10/t$ to represent the properties at $T \to 0$.

However, as λ_D is decreased sufficiently, $S_{\rm cdw}$ eventually shows no signal of LRO even at large β, providing an indication that there is a QCP, with CDW order occurring only above a finite λ_D value. Figure 6 also suggests that the critical temperature T_c is nonmonotonic with increasing λ_D. The values of β at which $S_{\rm cdw}$ grows first shift downward but then become larger again. This nonmonotonicity agrees with

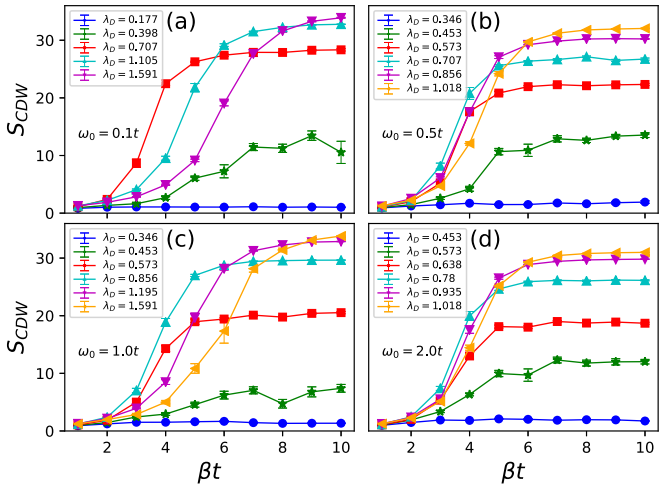

FIG. 6. The CDW structure factor of the π-flux phase Holstein model as a function of inverse temperature β. The phonon frequencies ω_0 are (a) $0.1t$, (b) $0.5t$, (c) $1.0t$, and (d) $2.0t$. The lattice size $L = 6$.

previous studies of Dirac fermions on the honeycomb lattice [37,38]. We can estimate the maximum T_c to occur at $\lambda_D \approx 0.71, 0.71, 0.86$, and 0.78 for $\omega_0 = 0.1t, 0.5t, 1.0t, 2.0t$, respectively. In the antiadiabatic limit $\omega_0 \to \infty$, the Holstein model maps onto the attractive Hubbard model, and $T_c = 0$ owing to the degeneracy of CDW and superconducting correlations [29]. (The order parameter has a continuous symmetry.) A recent study [48] has shown that $\omega_0 \gtrsim 10^2\, t$ is required to achieve the $-U$ Hubbard model limit, a surprisingly large value.

Figure 7(a) shows $S_{\rm cdw}$ as a function of λ at fixed $\omega_0 = 1.0t$. At the highest temperature shown, $\beta = 4/t$, $S_{\rm cdw}$ reaches a maximum at intermediate coupling $\lambda \sim 2.0$, then decreases as λ gets larger. The region for which $S_{\rm cdw}$ is large is a measure of the range of λ for which the CDW ordering temperature T_c exceeds β^{-1}. As β increases, this range is enlarged. Figure 7(b) is an analogous plot of $S_{\rm cdw}$ as a function of ω_0 at fixed $\lambda = 3.0$. The two plots appear as mirror images of each other since the dimensionless EPC $\lambda_D = \lambda^2/(\omega_0^2 W)$ increases with λ but decreases with ω_0.

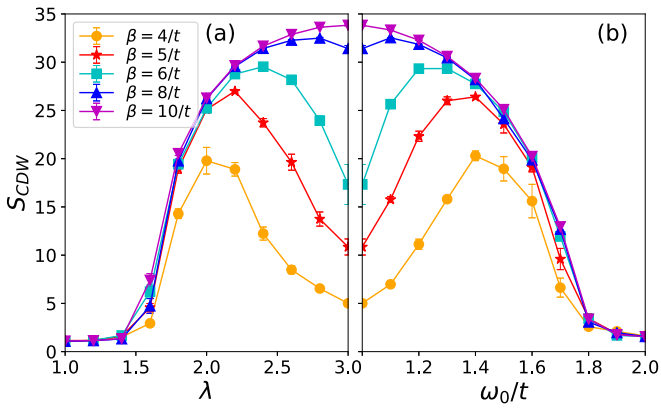

FIG. 7. $S_{\rm cdw}$ (a) as a function of λ at fixed $\omega_0 = 1.0t$ and (b) as a function of ω_0 at fixed $\lambda = 3.0$ at different inverse temperatures β. Lattice size $L = 6$ is used.

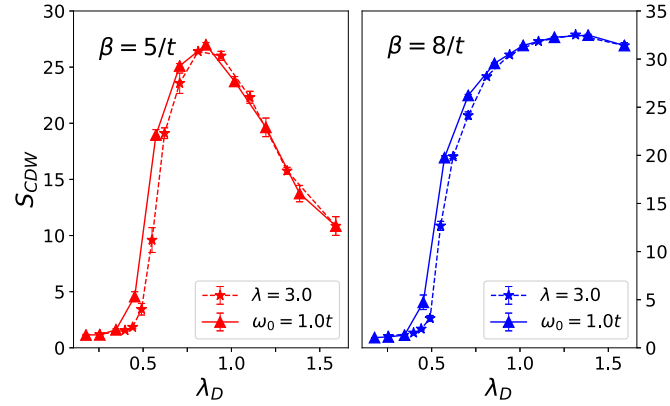

FIG. 8. Comparison of the evolution of $S_{\rm cdw}$ with coupling strength by changing λ or changing ω_0. Data are taken from Figs. 7(a) and 7(b) for $\beta = 5/t$ (left) and $\beta = 8/t$ (right). The difference is negligible at $\lambda_D > 0.8$ but not in the coupling regime $0.4 < \lambda_D < 0.8$ near the QCP.

It is interesting to ascertain the extent to which the physics of the Holstein Hamiltonian is determined by λ and ω_0 separately versus only the combination λ_D. Figure 8 addresses this issue by replotting the data in Figs. 7(a) and 7(b) as a function of λ_D for two values of the inverse temperature. For $\lambda_D \gtrsim 0.8$, the data collapse well, whereas at small λ_D, $S_{\rm cdw}$ can vary by as much as a factor of 2 even though λ_D is identical. It is likely that this sensitivity to the individual value of λ and ω_0 is associated with proximity to the QCP.

We compare the semimetal to CDW transition with increasing λ_D for the π-flux phase and honeycomb lattices in Fig. 9. These data are at lower temperatures than those in Fig. 8, so that the ground-state values of $S_{\rm cdw}$ have been reached for the system sizes shown.

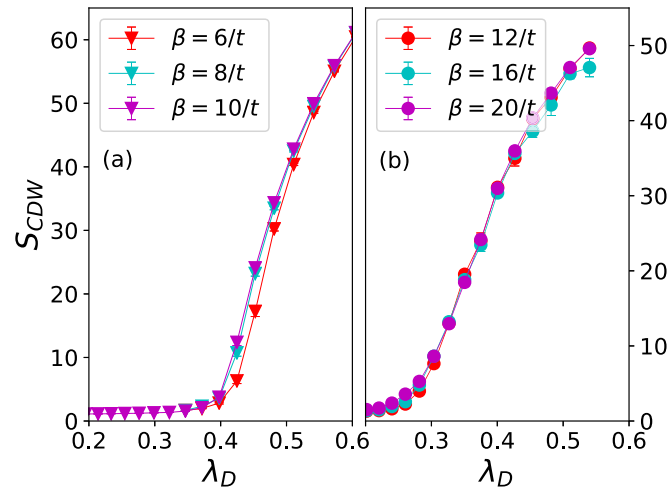

FIG. 9. $S_{\rm cdw}$ as a function of λ_D for (a) the π-flux phase square lattice and (b) honeycomb model. The lattice size $L = 6$ is used for both geometries. λ_D is varied by changing λ at fixed $\omega_0 = 1.0t$. $S_{\rm cdw}$ does not change for the lowest temperatures, indicating that the ground state has been reached for this finite lattice size.

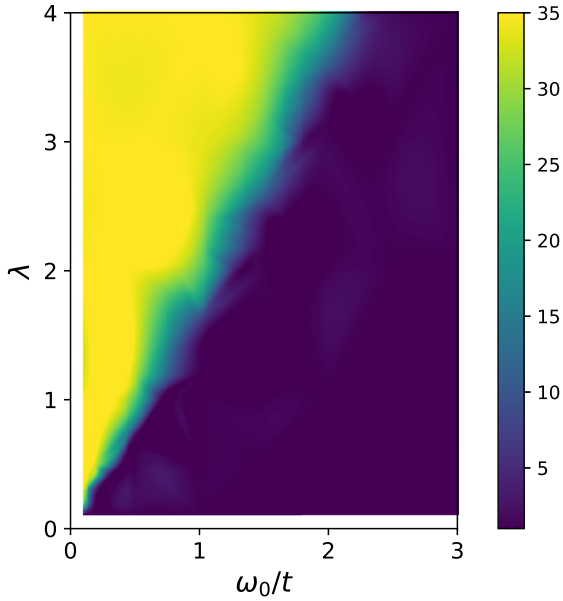

FIG. 10. Heat map of the ground state values of $S_{\rm cdw}$ in the (λ, ω_0) plane.

C. Ground state in the (λ, ω_0) plane

Figure 10 provides another perspective on the dependence of the CDW order on λ and ω_0 individually by giving a heat map of $S_{\rm cdw}$ in the (λ, ω_0) plane at low temperature. The bright yellow in top left indicates a strong CDW phase, whereas the dark purple region in the bottom right indicates the Dirac semimetal phase. The phase boundary is roughly linear, as would be expected if only the combination $\lambda_D = \lambda^2/(\omega_0^2 W)$ is relevant. We note, however, that this statement is only qualitatively true. The more precise line graphs of Fig. 8 indicate that along the line $\lambda = \sqrt{\lambda_{D,\rm crit} W}\,\omega_0 \sim 1.5\omega_0$, the separate values of λ and ω_0 are relevant.

D. Finite-size scaling: Finite-T transition

A quantitative determination of the finite temperature and quantum critical points can be done with finite-size scaling. Figure 11 gives both raw and scaled data for $S_{\rm cdw}$ for different lattice sizes $L = 4, 6, 8, 10$ at $\lambda = 2.0$, $\omega_0 = 1.0t$ as a function of β. Unscaled data are in Fig. 11(a): $S_{\rm cdw}$ is small and L independent at small β (high T) where $c(\mathbf{r})$ is short range. On the other hand, $S_{\rm cdw}$ is proportional to $N = L^2$ at large β (low T), reflecting the long-range CDW order in $c(\mathbf{r})$. Figure 11(b) shows a data crossing for different L occurs when $S_{\rm cdw}/L^{\gamma/\nu}$ is plotted versus β. A universal crossing is seen at $\beta t \sim 3.80 \pm 0.02$, giving a precise determination of critical temperature T_c. The two-dimensional Ising critical exponents $\gamma = 7/4$ and $\nu = 1$ were used in this analysis since the CDW phase transition breaks a similar discrete symmetry. Figure 11(c) shows a full data collapse when the β axis is also appropriately scaled by $L^{1/\nu}$. The best collapse occurs at $\beta_c = 3.80/t$, consistent with the result from the data crossing.

In the region immediately above the QCP, the DQMC values for T_c are roughly five times lower than those obtained in MFT, and indeed, the MFT overestimation of T_c can be made arbitrarily large at strong coupling. This reflects both the relatively low dimensionality ($d = 2$) and the fact that MFT fails to distinguish moment-forming and moment-ordering temperature scales.

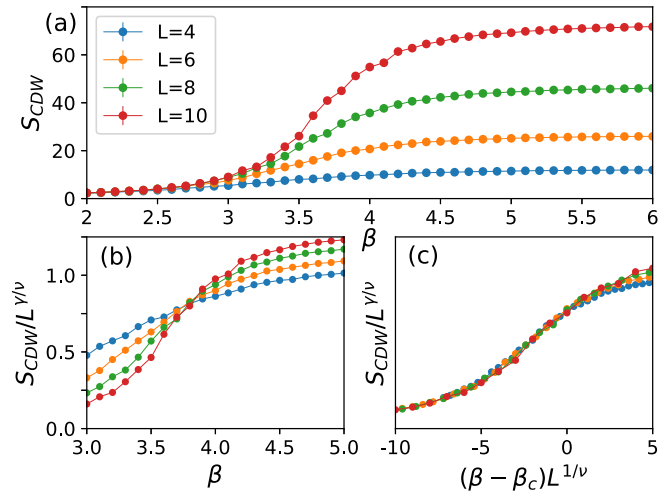

FIG. 11. (a) The CDW structure factor $S_{\rm cdw}$ as a function of β for several lattice sizes. (b) The scaled CDW structure factor $S_{\rm cdw}/L^{\gamma/\nu}$ as a function of β using Ising critical exponents $\gamma = 7/4$ and $\nu = 1$, showing a crossing of different L at $\beta_c = 3.80/t$. (c) $S_{\rm CDW}/L^{\gamma/\nu}$ versus $(\beta - \beta_c)L$, giving a best data collapse at $\beta_c = 3.80/t$. Here the parameters are $\lambda = 2.0$ and $\omega_0 = 1.0\,t$.

E. Quantum phase transition

Analysis of the renormalization group invariant Binder cumulant [49],

$$\mathcal{B} = \frac{3}{2}\left(1 - \frac{1}{3}\frac{< S_{\rm cdw}^2 >}{< S_{\rm cdw} >^2}\right), \tag{10}$$

can be used to locate the quantum critical point precisely. Only lattice sizes $L = 4n$, where n is an integer, can be used; for

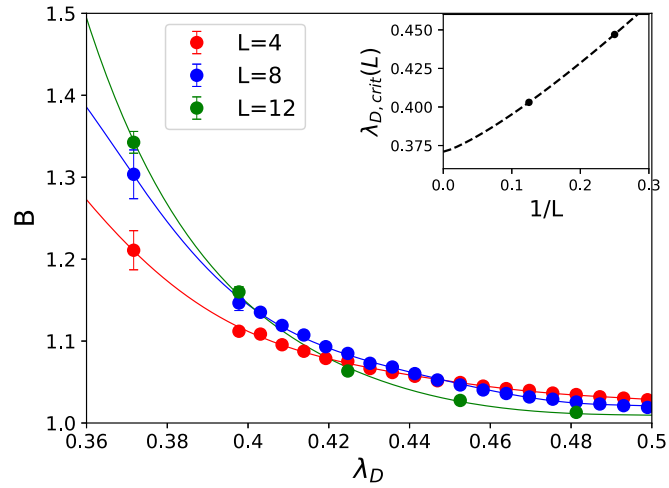

FIG. 12. Binder cumulant as a function of EPC strength λ_D for three lattice sizes. The inverse temperature is $\beta = 2\,L$, and ω_0 is fixed at $\omega_0 = 1.0t$. Inset: Extrapolation of the crossings for pairs of sizes as a function of $1/L$ to get the QCP in the thermodynamic limit.

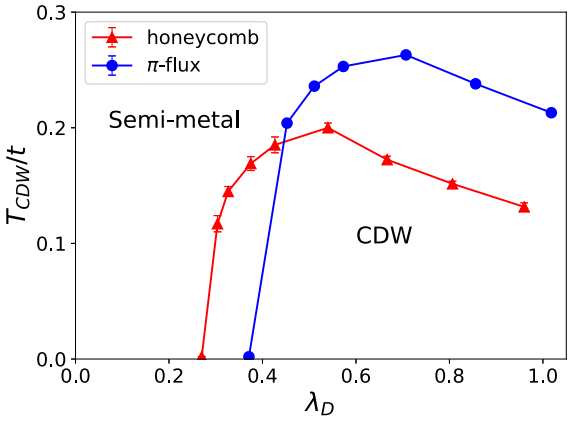

FIG. 13. Critical temperature T_c for the CDW phase transition, obtained from DQMC for both the π-flux phase square lattice (blue line) and the honeycomb lattice (red line), in a range of coupling strength. λ_D is varied by changing λ at fixed $\omega_0 = 1.0t$ for both models. The quantum critical point is determined using Binder cumulant analysis (discussed in the text). Data for the honeycomb lattice are taken from [37]. Error bars are smaller than symbol size for π-flux data.

other L the Dirac points are not any of the allowed $\mathbf{k}$ values, and finite-size effects are much more significant. As exhibited in Fig. 12, for $L = 4$, 8, and 12, $\mathcal{B}$ exhibits a set of crossings in a range about $\lambda_D \approx 0.4$. An extrapolation in $1/L$, as shown in the inset of Fig. 12, gives $\lambda_{D,\mathrm{crit}} = 0.371 \pm 0.003$.

F. Phase diagram

Location of the finite-temperature phase boundary (Fig. 11) and the QCP (Fig. 12) can be combined into the phase diagram of Fig. 13. Results for the π-flux geometry (blue circles) are put in better context by comparison with those of the honeycomb lattice (red triangles). Data were obtained at fixed $\omega_0 = 1.0t$. In both geometries, phase transitions into CDW order happen only above a finite $\lambda_{D,\mathrm{crit}}$. Beyond $\lambda_{D,\mathrm{crit}}$, T_c rises rapidly to its maximal value before decaying. For the π-flux model, T_c reaches a maximum $T_{c,\mathrm{max}}/t \sim 0.26$ at $\lambda_D \sim 0.7$, whereas for the honeycomb lattice T_c reaches its maximum $T_{c,\mathrm{max}}/t \sim 0.20$ at $\lambda_D \sim 0.5$. Similarly, $\lambda_{D,\mathrm{crit}}$ for π flux is larger than that of the honeycomb lattice, as $\lambda_{D,\mathrm{crit}} = 0.42$ and 0.27, respectively. When measured in terms of the relative Fermi velocities $v_\mathrm{F} = 2t, 1.5t$ for the π flux and honeycomb, respectively, these values become very similar: $\lambda_{D,\mathrm{crit}}/v_\mathrm{F} = 0.21$ and 0.18 for the π flux and honeycomb; $T_{c,\mathrm{max}}/v_\mathrm{F} = 0.13$ and 0.13.

VI. CONCLUSIONS

This paper has determined the quantitative phase diagram for Dirac fermions interacting with local phonon modes on the π-flux lattice. A key feature, shared with the honeycomb geometry, is the presence of a quantum critical point $\lambda_{D,\mathrm{crit}}$ below which the system remains a semimetal down to $T = 0$. The values of T_c and $\lambda_{D,\mathrm{crit}}$ for the two cases, when normalized to the Fermi velocities, agree to within roughly 10%.

We have also considered the question of whether the properties of the model can be described in terms of the single ratio λ^2/ω_0^2. We find that qualitatively, this is, indeed, the case but that, quantitatively, the charge structure factor can depend significantly on the individual values of EPC and phonon frequency, especially in the vicinity of the QCP. However, this more complex behavior is masked by the fact that T_c rises so rapidly with λ in that region. In investigating this issue we have studied substantially smaller values of ω_0 than have typically been investigated in QMC treatments of the Holstein Hamiltonian.

ACKNOWLEDGMENTS

The work of Y.-X.Z. and R.T.S. was supported by the Grant No. DE-SC0014671 funded by the US Department of Energy, Office of Science. H.-M.G. was supported by NSFC Grant No. 11774019. The authors would like to thank B. Cohen-Stead and W.-T. Chiu for useful conversations.

[1] A. H. Castro Neto, F. Guinea, N. M. R. Peres, K. S. Novoselov, and A. K. Geim, The electronic properties of graphene, Rev. Mod. Phys. **81**, 109 (2009).
[2] A. K. Geim, Graphene: Status and prospects, Science **324**, 1530 (2009).
[3] W. Choi, I. Lahiri, R. Seelaboyina, and Y. S. Kang, Synthesis of graphene and its applications: A review, Crit. Rev. Solid State Mater. Sci. **35**, 52 (2010).
[4] K. S. Novoselov, V. I. Fal, L. Colombo, P. R. Gellert, M. G. Schwab, K. Kim *et al.*, A roadmap for graphene, Nature (London) **490**, 192 (2012).
[5] A. B. Harris, T. C. Lubensky, and E. J. Mele, Flux phases in two-dimensional tight-binding models, Phys. Rev. B **40**, 2631 (1989).
[6] Y. Jia, H. Guo, Z. Chen, S.-Q. Shen, and S. Feng, Effect of interactions on two-dimensional Dirac fermions, Phys. Rev. B **88**, 075101 (2013).
[7] Y. Otsuka and Y. Hatsugai, Mott transition in the two-dimensional flux phase, Phys. Rev. B **65**, 073101 (2002).
[8] Y. Otsuka, S. Yunoki, and S. Sorella, Mott transition in the 2D Hubbard model with π-flux, JPS Conf. Proc. **3**, 013021 (2014).
[9] Z.-X. Li, Y.-F. Jiang, and H. Yao, Fermion-sign-free Majarana-quantum-Monte-Carlo studies of quantum critical phenomena of Dirac fermions in two dimensions, New J. Phys. **17**, 085003 (2015).
[10] F. P. Toldin, M. Hohenadler, F. F. Assaad, and I. F. Herbut, Fermionic quantum criticality in honeycomb and π-flux Hubbard models: Finite-size scaling of renormalization-group-invariant observables from quantum Monte Carlo, Phys. Rev. B **91**, 165108 (2015).
[11] Y. Otsuka, S. Yunoki, and S. Sorella, Universal Quantum Criticality in the Metal-Insulator Transition of Two-Dimensional Interacting Dirac Electrons, Phys. Rev. X **6**, 011029 (2016).

[12] T. C. Lang and A. M. Läuchli, Quantum Monte Carlo Simulation of the Chiral Heisenberg Gross-Neveu-Yukawa Phase Transition with a Single Dirac Cone, Phys. Rev. Lett. **123**, 137602 (2019).

[13] H.-M. Guo, L. Wang, and R. T. Scalettar, Quantum phase transitions of multispecies Dirac fermions, Phys. Rev. B **97**, 235152 (2018).

[14] H. Guo, E. Khatami, Y. Wang, T. P. Devereaux, R. R. P. Singh, and R. T. Scalettar, Unconventional pairing symmetry of interacting Dirac fermions on a π-flux lattice, Phys. Rev. B **97**, 155146 (2018).

[15] L. Wang, P. Corboz, and M. Troyer, Fermionic quantum critical point of spinless fermions on a honeycomb lattice, New J. Phys. **16**, 103008 (2014).

[16] Z. Y. Meng, T. C. Lang, S. Wessel, F. F. Assaad, and A. Muramatsu, Quantum spin liquid emerging in two-dimensional correlated Dirac fermions, Nature (London) **464**, 847 (2010).

[17] Y. Otsuka, S. Yunoki, and S. Sorella, Quantum Monte Carlo study of the half-filled Hubbard model on the honeycomb lattice, J. Phys.: Conf. Series **454**, 012045 (2013).

[18] Z. Zhou, C. Wu, and Y. Wang, Mott transition in the π-flux $su(4)$ Hubbard model on a square lattice, Phys. Rev. B **97**, 195122 (2018).

[19] C.-C. Chang and R. T. Scalettar, Quantum Disordered Phase Near the Mott Transition in the Staggered-Flux Hubbard Model on a Square Lattice, Phys. Rev. Lett. **109**, 026404 (2012).

[20] T. Holstein, Studies of polaron motion: Part I. the molecular-crystal model, Ann. Phys. (N.Y.) **8**, 325 (1959).

[21] P. E. Kornilovitch, Continuous-Time Quantum Monte Carlo Algorithm for the Lattice Polaron, Phys. Rev. Lett. **81**, 5382 (1998).

[22] P. E. Kornilovitch, Ground-state dispersion and density of states from path-integral Monte Carlo: Application to the lattice polaron, Phys. Rev. B **60**, 3237 (1999).

[23] A. S. Alexandrov, Polaron dynamics and bipolaron condensation in cuprates, Phys. Rev. B **61**, 12315 (2000).

[24] M. Hohenadler, H. G. Evertz, and W. von der Linden, Quantum Monte Carlo and variational approaches to the Holstein model, Phys. Rev. B **69**, 024301 (2004).

[25] L.-C. Ku, S. A. Trugman, and J. Bonča, Dimensionality effects on the Holstein polaron, Phys. Rev. B **65**, 174306 (2002).

[26] P. E. Spencer, J. H. Samson, P. E. Kornilovitch, and A. S. Alexandrov, Effect of electron-phonon interaction range on lattice polaron dynamics: A continuous-time quantum Monte Carlo study, Phys. Rev. B **71**, 184310 (2005).

[27] A. Macridin, G. A. Sawatzky, and M. Jarrell, Two-dimensional Hubbard-Holstein bipolaron, Phys. Rev. B **69**, 245111 (2004).

[28] A. H. Romero, D. W. Brown, and K. Lindenberg, Effects of dimensionality and anisotropy on the Holstein polaron, Phys. Rev. B **60**, 14080 (1999).

[29] R. T. Scalettar, N. E. Bickers, and D. J. Scalapino, Competition of pairing and Peierls–charge-density-wave correlations in a two-dimensional electron-phonon model, Phys. Rev. B **40**, 197 (1989).

[30] F. Marsiglio, Pairing and charge-density-wave correlations in the Holstein model at half-filling, Phys. Rev. B **42**, 2416 (1990).

[31] M. Vekic, R. M. Noack, and S. R. White, Charge-density waves versus superconductivity in the Holstein model with next-nearest-neighbor hopping, Phys. Rev. B **46**, 271 (1992).

[32] P. Niyaz, J. E. Gubernatis, R. T. Scalettar, and C. Y. Fong, Charge-density-wave-gap formation in the two-dimensional Holstein model at half-filling, Phys. Rev. B **48**, 16011 (1993).

[33] M. Vekić and S. R. White, Gap formation in the density of states for the Holstein model, Phys. Rev. B **48**, 7643 (1993).

[34] J. K. Freericks, M. Jarrell, and D. J. Scalapino, Holstein model in infinite dimensions, Phys. Rev. B **48**, 6302 (1993).

[35] H. Zheng and S. Y. Zhu, Charge-density-wave and superconducting states in the Holstein model on a square lattice, Phys. Rev. B **55**, 3803 (1997).

[36] E. Jeckelmann, C. Zhang, and S. R. White, Metal-insulator transition in the one-dimensional Holstein model at half filling, Phys. Rev. B **60**, 7950 (1999).

[37] Y.-X. Zhang, W.-T. Chiu, N. C. Costa, G. G. Batrouni, and R. T. Scalettar, Charge Order in the Holstein Model on a Honeycomb Lattice, Phys. Rev. Lett. **122**, 077602 (2019).

[38] C. Chen, X. Y. Xu, Z. Y. Meng, and M. Hohenadler, Charge-Density-Wave Transitions of Dirac Fermions Coupled to Phonons, Phys. Rev. Lett. **122**, 077601 (2019).

[39] I. Affleck and J. B. Marston, Large-n limit of the Heisenberg-Hubbard model: Implications for high-T_c superconductors, Phys. Rev. B **37**, 3774 (1988).

[40] M. Aidelsburger, M. Atala, S. Nascimbene, S. Trotzky, Y.-A. Chen, and I. Bloch, Experimental Realization of Strong Effective Magnetic Fields in an Optical Lattice, Phys. Rev. Lett. **107**, 255301 (2011).

[41] S. Gazit, M. Randeria, and A. Vishwanath, Emergent Dirac fermions and broken symmetries in confined and deconfined phases of Z_2 gauge theories, Nat. Phys. **13**, 484 (2017).

[42] E. H. Lieb, Flux Phase of the Half-Filled Band, Phys. Rev. Lett. **73**, 2158 (1994).

[43] G. Mazzucchi, L. Lepori, and A. Trombettoni, Semimetal–superfluid quantum phase transitions in 2D and 3D lattices with Dirac points, J. Phys. B **46**, 134014 (2013).

[44] Y.-J. Wu, J. Zhou, and S.-P. Kou, Strongly fluctuating fermionic superfluid in the attractive π-flux Hubbard model, Phys. Rev. A **89**, 013619 (2014).

[45] R. Blankenbecler, D. J. Scalapino, and R. L. Sugar, Monte Carlo calculations of coupled boson-fermion systems. I, Phys. Rev. D **24**, 2278 (1981).

[46] S. R. White, D. J. Scalapino, R. L. Sugar, E. Y. Loh, J. E. Gubernatis, and R. T. Scalettar, Numerical study of the two-dimensional Hubbard model, Phys. Rev. B **40**, 506 (1989).

[47] E. Y. Loh, J. E. Gubernatis, R. T. Scalettar, S. R. White, D. J. Scalapino, and R. L. Sugar, Sign problem in the numerical simulation of many-electron systems, Phys. Rev. B **41**, 9301 (1990).

[48] C. Feng, H. Guo, and R. T. Scalettar, Charge density waves on a decorated honeycomb lattice, Phys. Rev. B **101**, 205103 (2020).

[49] K. Binder, Finite size scaling analysis of Ising model block distribution functions, Z. Phys. B **43**, 119 (1981).